Energy &
Environmental
Science

ROYAL SOCIETY
OF CHEMISTRY

COMMUNICATION

View Article Online
View Journal | View Issue

Check for updates

Cite this: *Energy Environ. Sci.*, 2023, **16**, 3753

Received 8th May 2023,
Accepted 31st July 2023

DOI: 10.1039/d3ee01450a

rsc.li/ees

A giant Nernst power factor and figure-of-merit in polycrystalline $NbSb_2$ for Ettingshausen refrigeration†

Peng Li,[ab] Pengfei Qiu,*[abc] Jie Xiao,[a] Tingting Deng,[c] Lidong Chen[ab] and Xun Shi*[ab]

Ettingshausen refrigeration is a promising solid-state refrigeration technology that can be used in exploring the quantum state of matters and superconducting materials, but its development is greatly limited by the lack of high-performance polycrystalline thermomagnetic materials. In this work, we report that the polycrystalline topological semimetal $NbSb_2$ has a giant Nernst power factor ($(PF)_N$) of 1269 × 10^{-4} W m^{-1} K^{-2} under 9 T at 28 K and a Nernst figure-of-merit (z_N) of 28.5 × 10^{-4} K^{-1} under 9 T at 18 K, both of which are record-high values among the polycrystalline thermomagnetic materials. The observed high thermomagnetic performance is mainly attributed to the large and unsaturated Nernst thermopower under a high magnetic field. Due to the diminished anisotropy, the polycrystalline $NbSb_2$ has similar high carrier mobility to the single-crystalline $NbSb_2$ in the *bc*-plane, yielding large Nernst thermopower in low temperature ranges. Combining the excellent thermomagnetic performance and low-cost and time-saving fabrication process, polycrystalline $NbSb_2$ is a very competitive candidate material for Ettingshausen refrigeration.

Broader context

The demand for thermoelectric applications at low temperatures is heightened now by the exploration of quantum state of matters, quantum information science, and space science. However, today good thermoelectric and thermomagnetic materials in the low temperature range, particularly at temperatures below the liquid nitrogen boiling point, are still very rare. Discovering high performance thermoelectric and thermomagnetic materials below the liquid nitrogen temperature has become a very active field worldwide. In this work, we demonstrate that polycrystalline $NbSb_2$ has a giant Nernst power factor of 1269 × 10^{-4} W m^{-1} K^{-2} under 9 T at 28 K and a Nernst figure-of-merit of 28.5 × 10^{-4} K^{-1} under 9 T at 18 K. These values are not only the highest among the polycrystalline thermomagnetic materials, but are also superior to many single-crystalline thermomagnetic materials reported before. More importantly, polycrystalline $NbSb_2$ can be easily synthesized by using a low-cost and time-saving fabrication process, which is more competitive than the single-crystalline thermomagnetic materials for the fabrication of an Ettingshausen refrigerator. This work provides a new optional material for solid-state heat pumping below liquid nitrogen temperature based on Ettingshausen refrigeration.

Introduction

A low-temperature environment is essential for the investigation of quantum states of matter,[1] superconducting materials,[2] and space science.[3] Beyond the traditional compressor refrigerator based on gaseous working substances, thermoelectric (TE) refrigeration provides an alternative way to obtain a low-temperature environment.[4–7] When a current flows through the thermoelectric (TE) device, the temperature at one end of the device can be reduced. According to the working principle, TE refrigeration can be divided into two categories, termed as Peltier refrigeration and Ettingshausen refrigeration.[8] Besides the electric current, the latter one also needs the assistance of a magnetic field.

Compared with Peltier refrigeration, which has already realized commercialization several decades before,[4,5] the development of Ettingshausen refrigeration is relatively slow. The main reason is the lack of high performance thermomagnetic materials with a high Nernst power factor ($(PF)_N = {S_{yx}}^2\sigma_{yy}$, determining the transverse pumping power, where S_{yx} is the Nernst thermopower and σ_{yy} is the longitudinal electrical conductivity) and large Nernst figure-of-merit ($z_N = {S_{yx}}^2\sigma_{yy}/\kappa_{xx}$, determining the maximum temperature gradient that can be built across the device, where κ_{xx} is the transverse thermal conductivity).[8] To maximize $(PF)_N$ and z_N, the material for Ettingshausen refrigeration requires electrons and holes possessing

---

[a] State Key Laboratory of High Performance Ceramics and Superfine Microstructure, Shanghai Institute of Ceramics, Chinese Academy of Science, Shanghai 200050, China. E-mail: qiupf@mail.sic.ac.cn, xshi@mail.sic.ac.cn

[b] Center of Materials Science and Optoelectronics Engineering, University of Chinese Academy of Sciences, Beijing 100049, China

[c] School of Chemistry and Materials Science, Hangzhou Institute for Advanced Study, University of Chinese Academy of Sciences, Hangzhou 310024, China

† Electronic supplementary information (ESI) available. See DOI: https://doi.org/10.1039/d3ee01450a

nearly identical concentrations and high mobilities, which greatly limit the scope of optional materials.[9] Thus, for a long time, the investigation of Ettingshausen refrigeration was limited in a few thermomagnetic materials (*e.g.* Bi–Sb alloys[10,11] and In–Sb alloys[12]). The peak $(PF)_N$ and z_N are about 324×10^{-4} W m^{-1} K^{-2} and 55×10^{-4} K^{-1} for single-crystalline $Bi_{97}Sb_3$ under 1 T at 115 K, respectively.[10]

Recently, the investigation of Ettingshausen refrigeration was rejuvenated due to the great progress achieved in topological semimetals.[13–15] A series of topological semimetals have been reported with high thermomagnetic performance, such as Cd_3As_2,[16] $ZrTe_5$,[17] $PtSn_4$,[18] Mg_2Pb,[19] $NbSb_2$,[20] and WTe_2.[21] Some of them exhibit superior $(PF)_N$ to the Bi–Sb alloys, such as 425×10^{-4} W m^{-1} K^{-2} for single-crystalline Mg_2Pb under 10 T at 30 K,[19] 3800×10^{-4} W m^{-1} K^{-2} for single-crystalline $NbSb_2$ under 5 T at 25 K,[20] and 3 W m^{-1} K^{-2} for single-crystalline WTe_2 under 9 T at 11.3 K.[21] The maximum z_N of thermomagnetic materials was boosted up to 265×10^{-4} K^{-1} for single-crystalline WTe_2 under 9 T at 11.3 K.[21] However, all these high $(PF)_N$ and z_N are achieved in single crystals, in which the preparation methods are usually time-consuming and expensive. Furthermore, the crystal sizes are usually small, which greatly limit the real application of Ettingshausen refrigeration. In contrast to single crystals, the polycrystals can be easily prepared into large bulks by using simple and low-cost preparation methods, which are more suitable for real application. However, currently the investigation on polycrystalline thermomagnetic materials is very rare.[22–25] Particularly, as shown in Fig. 1, the $(PF)_N$ and z_N of the reported polycrystalline thermomagnetic materials are much lower than those of single-crystalline thermomagnetic materials. Discovering the polycrystalline thermomagnetic materials with high $(PF)_N$ and z_N has already become an important task for the investigation of Ettingshausen refrigeration.

In this work, we report the discovery of a colossal $(PF)_N$ of 1269×10^{-4} W m^{-1} K^{-2} under 9 T at 28 K and a high z_N of 28.5×10^{-4} K^{-1} under 9 T at 18 K in polycrystalline $NbSb_2$, both of which are record-high values in polycrystalline thermomagnetic materials (Fig. 1). The excellent performance of polycrystalline $NbSb_2$ is caused by the nearly identical electron and hole concentrations near the Fermi level, ultrahigh mobilities close to 1 m^2 V^{-1} s^{-1}, and a strong phonon-drag effect in low temperature ranges. This work provides a novel potential candidate material for Ettingshausen refrigeration.

Results and discussion

Polycrystalline $NbSb_2$ was fabricated by using the solid-state reaction and spark plasma sintering technique. Fig. 2a shows the powder X-ray diffraction pattern of polycrystalline $NbSb_2$. All diffraction peaks can be indexed belonging to the centrosymmetric monoclinic structure (space group C_2/m) of $NbSb_2$ (the inset in Fig. 2a). Backscattered electron (BSE) image (Fig. 2b) and energy dispersive X-ray spectroscopy (EDS) mapping (Fig. 2c and d) indicate that Nb and Sb are homogeneously distributed inside the matrix, confirming that the prepared polycrystalline $NbSb_2$ is phase pure. Fig. 2e shows that the grain sizes are about several micrometers. No obvious orientation is observed. Such high homogeneity and isotropy provide the basis for the accurate measurement of thermomagnetic performance in this work.

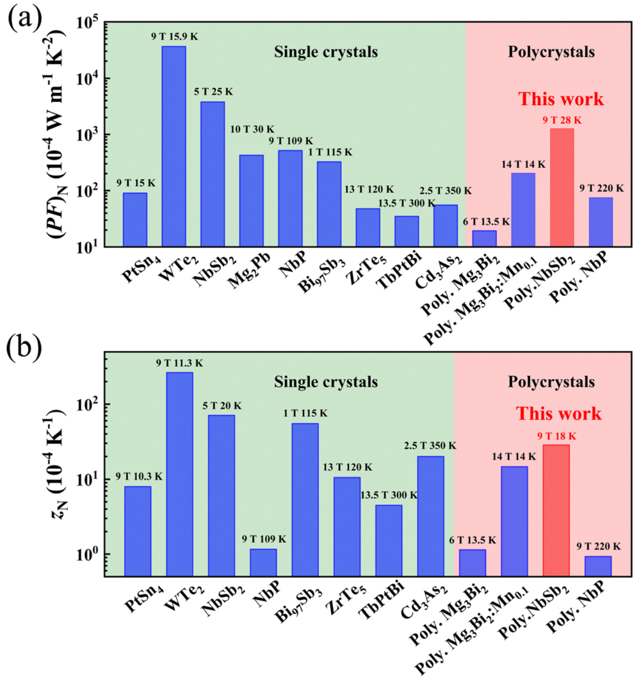

Fig. 1 (a) Comparisons of the (a) Nernst power factor $(PF)_N$ and (b) Nernst figure-of-merit z_N of polycrystalline $NbSb_2$ and some typical thermomagnetic materials reported before.[10,16–21,23–28] The maximum $(PF)_N$ and z_N of each thermomagnetic material are used in the figures.

Fig. 3a shows the temperature dependence of the Seebeck thermopower S_{xx} of polycrystalline $NbSb_2$ under different magnetic fields B. In the absence of a magnetic field, the S_{xx} of polycrystalline $NbSb_2$ below 100 K is almost zero. This is consistent with the band structure of $NbSb_2$, with the schematics shown in the inset of Fig. 3a. The Fermi level crosses both the valence and conduction bands, demonstrating a typical feature of semimetals. Above 100 K, the S_{xx} decreases linearly with increasing temperature, reaching −20 μV K^{-1} at 300 K. When the magnetic field is applied, the S_{xx} below 100 K is significantly enhanced, while that above 100 K is only slightly increased. Similar temperature-dependence and magnetic field-dependence have been also observed in single-crystalline $NbSb_2$,[20] indicating that the grain boundary has little influence on the S_{xx}.

Fig. 3b shows the temperature dependence of the Nernst thermopower S_{yx} of polycrystalline $NbSb_2$ under different magnetic fields B. Under each magnetic field, the absolute value of S_{yx} firstly increases with the increase of temperature, reaching a peak around 21 K, and then decreases for higher temperature. Likewise, with the increase of magnetic field, the S_{yx} is monotonously increased, which can be more intuitively reflected in Fig. S2 (ESI†). Under the same magnetic field and temperature, the S_{yx} of polycrystalline $NbSb_2$ is smaller than that of single-crystalline $NbSb_2$. For example, the S_{yx} of polycrystalline $NbSb_2$ is 396 μV K^{-1} under 9 T at 21 K, which is 36%

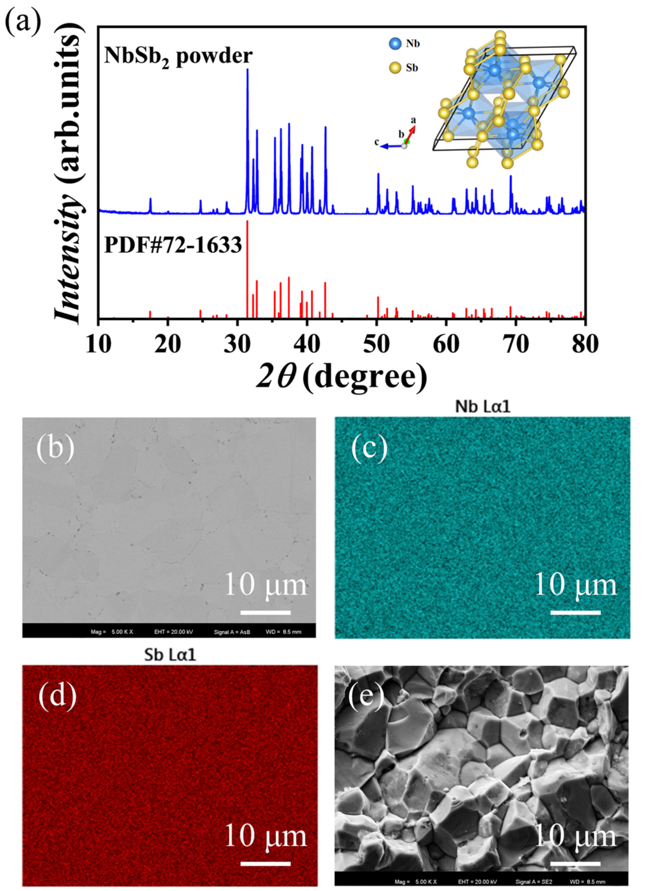

Fig. 2 (a) Powder X-ray diffraction pattern for polycrystalline $NbSb_2$. The inset shows the crystal structure of $NbSb_2$. (b) Backscattered electron (BSE) image and (c) and (d) energy dispersive X-ray spectroscopy (EDS) mapping performed on polycrystalline $NbSb_2$. (e) Cross-section image of fractured polycrystalline $NbSb_2$.

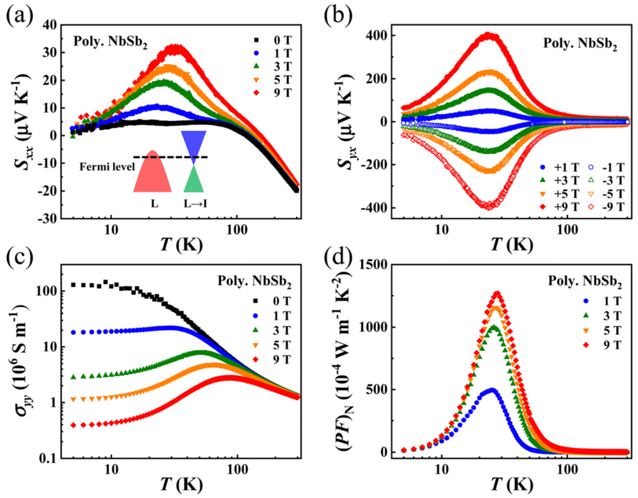

Fig. 3 Temperature dependences of (a) Seebeck thermopower S_{xx}, (b) Nernst thermopower S_{yx}, (c) electrical conductivity σ_{yy}, and (d) Nernst power factor $(PF)_N$ for polycrystalline $NbSb_2$ under different magnetic fields. The inset in (a) represents the schematics of the band structure of $NbSb_2$ near the Fermi level.

lower than that of single-crystalline $NbSb_2$ (616 $\mu V\ K^{-1}$) under the same conditions.[20] Thus, the grain boundaries in polycrystalline $NbSb_2$ lead to decreased S_{yx}.

To obtain the Nernst power factor $(PF)_N$, a longitudinal electrical conductivity σ_{yy} is required. Under a magnetic field, the motion of the carriers is deflected by the Lorentz force. The motion of the carriers is subject to the influence from other directions. In this case, the σ_{yy} of polycrystalline $NbSb_2$ can be described as[29]

$$\sigma_{yy} = \frac{\rho_{xx}}{{\rho_{xx}}^2 + {\rho_{yx}}^2} \qquad (1)$$

where ρ_{xx} is the transverse electrical resistivity and ρ_{yx} is the Hall resistivity. In the absence of magnetic field, the ρ_{xx} of polycrystalline $NbSb_2$ increases with increasing temperature, which is consistent with the semimetal feature of $NbSb_2$ (Fig. S3a, ESI†). When the magnetic field is applied, the ρ_{xx} is significantly enhanced, particularly below 100 K, indicating the existence of a strong magnetoresistance effect. The ρ_{yx} shown in Fig. S3b (ESI†) is negative over the entire temperature range, indicating that the dominant carriers are electrons in polycrystalline $NbSb_2$. Under the same magnetic field and temperature, $|\rho_{yx}|$ is much smaller than ρ_{xx}, indicating that the contributions of electrons and holes in the electrical transports are close. Fig. 3c shows the calculated σ_{yy} for polycrystalline $NbSb_2$. The temperature-dependence and magnetic field-dependence are similar to those of single-crystalline $NbSb_2$, but the value is slightly lower than that of single-crystalline $NbSb_2$ under the same magnetic field and temperature. For example, the σ_{yy} of polycrystalline $NbSb_2$ is $0.65 \times 10^6\ S\ m^{-1}$ under 9 T at 21 K, which is 20% lower than that of single-crystalline $NbSb_2$ ($0.81 \times 10^6\ S\ m^{-1}$) under the same conditions.[20]

Based on the S_{yx} and σ_{yy}, the $(PF)_N$ of polycrystalline $NbSb_2$ is calculated and plotted in Fig. 3d. Due to the significantly enhanced S_{yx}, the $(PF)_N$ is also greatly increased upon applying magnetic field. When $B = 9$ T, the peak $(PF)_N$ of polycrystalline $NbSb_2$ is $1269 \times 10^{-4}\ W\ m^{-1}\ K^{-2}$ at 28 K. Likewise, Fig. S4 (ESI†) shows that the $(PF)_N$ tends to become saturated above 9 T, and thus further increasing the magnetic field will not significantly increase the $(PF)_N$. The peak $(PF)_N$ of polycrystalline $NbSb_2$ is a very exciting result since it is a record-high value among the polycrystalline thermomagnetic materials (Fig. 1a and Fig. S5, ESI†). Actually, this value is even higher than most single-crystalline thermomagnetic materials, such as single-crystalline $Bi_{97}Sb_3$,[10] Cd_3As_2,[16] $ZrTe_5$,[17] $PtSn_4$,[18] Mg_2Pb,[19] and $TbPtBi$[28] (Fig. 1a and Fig. S5, ESI†), and thermoelectric materials, such as Bi_2Te_3-based alloys,[30,31] $AgSbTe_2$,[32] $TaSiTe_4$,[33] and Ag_2S-based materials.[34–36]

The high $(PF)_N$ of polycrystalline $NbSb_2$ is mainly contributed by the large S_{yx}. Although the peak S_{yx} of polycrystalline $NbSb_2$ is lower than the single-crystalline $NbSb_2$, it is still much higher than most thermomagnetic materials reported before, such as 124 $\mu V\ K^{-1}$ for polycrystalline NbP under 9 T at 140 K,[23] 127 $\mu V\ K^{-1}$ for polycrystalline Mg_3Bi_2 under 13 T at 13.5 K,[24] 125 $\mu V\ K^{-1}$ for single-crystalline Cd_3As_2 under 3 T at 350 K,[16] 45 $\mu V\ K^{-1}$ for single-crystalline $PtSn_4$ under 9 T at 10.3 K,[18] 200 μV K^{-1} for single-crystalline Mg_2Pb under 10 T at 30 K,[19] and 225 μV K^{-1} for single-crystalline TbPtBi under 14 T at 240 K.[28] One main reason for the large S_{yx} is originated from its unsaturated behavior under a high magnetic field. As shown in Fig. S2 (ESI†), the S_{yx} linearly increases with increasing magnetic field, without showing obvious deflection even under 9 T.

When both the electrons and holes take part in electrical transports, the S_{yx} can be expressed as[37]

$$S_{yx} = \frac{\sigma_{xx}^{\mathrm{e}}\sigma_{xx}^{\mathrm{h}}(\mu_{\mathrm{e}}+\mu_{\mathrm{h}})B}{\left(\sigma_{xx}^{\mathrm{e}}+\sigma_{xx}^{\mathrm{h}}\right)^2}\left(S_{xx}^{\mathrm{h}}-S_{xx}^{\mathrm{e}}\right) \tag{2}$$

where σ_{xx}^{e} and σ_{xx}^{h} are the electrical conductivity contributed by electrons and holes, S_{xx}^{e} and S_{xx}^{h} are the Seebeck thermopower of electrons and holes under the magnetic field, μ_{e} and μ_{h} are electron mobility and hole mobility, respectively. n_{e} (or n_{h}) and μ_{e} (or μ_{h}) can be estimated by using the two-carrier model to fit the measured $\rho_{xx}(B)$ and $\rho_{yx}(B)$[38]

$$\rho_{xx}(B) = \frac{1}{\mathrm{e}}\frac{(n_{\mathrm{h}}\mu_{\mathrm{h}}+n_{\mathrm{e}}\mu_{\mathrm{e}})+(n_{\mathrm{h}}\mu_{\mathrm{e}}+n_{\mathrm{e}}\mu_{\mathrm{h}})\mu_{\mathrm{e}}\mu_{\mathrm{h}}B^2}{(n_{\mathrm{h}}\mu_{\mathrm{h}}+n_{\mathrm{e}}\mu_{\mathrm{e}})^2+(n_{\mathrm{h}}-n_{\mathrm{e}})^2{\mu_{\mathrm{e}}}^2{\mu_{\mathrm{h}}}^2B^2} \tag{3}$$

$$\rho_{yx}(B) = \frac{B\left(n_{\mathrm{h}}{\mu_{\mathrm{h}}}^2-n_{\mathrm{e}}{\mu_{\mathrm{e}}}^2\right)+(n_{\mathrm{h}}-n_{\mathrm{e}}){\mu_{\mathrm{e}}}^2{\mu_{\mathrm{h}}}^2B^2}{\mathrm{e}\left(n_{\mathrm{h}}\mu_{\mathrm{h}}+n_{\mathrm{e}}\mu_{\mathrm{e}}\right)^2+(n_{\mathrm{h}}-n_{\mathrm{e}})^2{\mu_{\mathrm{e}}}^2{\mu_{\mathrm{h}}}^2B^2} \tag{4}$$

Fig. S6 (ESI†) plots the $\rho_{xx}(B)$ and $\rho_{yx}(B)$ for polycrystalline $NbSb_2$ under different temperatures and magnetic field. At low temperatures (below 100 K), $\rho_{xx}(B)$ varies with the magnetic field B by a factor of 2 and $\rho_{yx}(B)$ also significantly deviates off linearity as B increases, which is consistent with the scenario described using eqn (3) and (4) when $\mu B \gg 1$. At high temperatures (above 100 K), the $\rho_{xx}(B)$ and $\rho_{yx}(B)$ exhibit weak magnetic field dependence since the decreased carrier mobility at high temperatures reduces the contribution of the nonlinear terms in eqn (3) and (4). The fitted n_{e} and n_{h} of polycrystalline $NbSb_2$ are very close in the whole temperature range (Fig. 4a). A similar phenomenon was also observed in single-crystalline $NbSb_2$.[20] This is consistent with the band structure of $NbSb_2$, which shows that the electron pocket and hole pocket near the Fermi level have nearly the same volume. Likewise, the fitted μ_{e} and μ_{h} of polycrystalline $NbSb_2$ are also very close in the whole temperature range (Fig. 4b). In this case, eqn (2) can be simplified into

$$S_{yx} = \frac{\bar{\mu}B}{2}\left(S_{xx}^{\mathrm{h}}-S_{xx}^{\mathrm{e}}\right) \tag{5}$$

where S_{yx} is in proportional to B. This can well explain the observed unsaturated behavior of S_{yx} under a high magnetic field for polycrystalline $NbSb_2$.

Beyond the high magnetic field, eqn (5) indicates that the high carrier mobility is also necessary for the large S_{yx}. The μ_{e} and μ_{h} of polycrystalline $NbSb_2$ are about 1.7 m^2 V^{-1} s^{-1} and 1.2 m^2 V^{-1} s^{-1} at 5 K, which are quite high values among those for the reported thermomagnetic materials, such as Cd_3As_2 (μ_{e} = 6.5 m^2 V^{-1} s^{-1}, μ_{h} = 0.5 m^2 V^{-1} s^{-1} at 10 K)[16], $PtSn_4$ (μ_{e} = 7.6 m^2 V^{-1} s^{-1}, μ_{h} = 7.6 m^2 V^{-1} s^{-1} at 10 K),[18] Mg_3Bi_2 (μ_{e} = 0.48 m^2 V^{-1} s^{-1}, μ_{h} = 0.14 m^2 V^{-1} s^{-1} at 15 K),[24] and TbPtBi (μ_{e} = 0.3 m^2 V^{-1} s^{-1}, μ_{h} = 0.3 m^2 V^{-1} s^{-1} at 20 K).[28] Generally, it is considered that the polycrystals have lower carrier mobility than the single crystals due to the additional grain boundary scattering to carriers. Interestingly, herein the polycrystalline $NbSb_2$ have similar μ_{e} and μ_{h} with the single-crystalline $NbSb_2$ in the *bc*-plane. This abnormal phenomenon is related to the anisotropic transport properties of single crystalline $NbSb_2$ at low temperatures. Herein, we measured the angular dependence of the resistivity ρ of single-crystalline $NbSb_2$ under a magnetic field to investigate the anisotropy. As shown in Fig. S7a and b (ESI†), for the single-crystalline $NbSb_2$, the angle between the magnetic field and the normal to the *bc*-plane is noted as θ. When $\theta = 0°$, the position of the magnetic field is perpendicular to the *bc*-plane. This is the condition used to measure the carrier mobility of single-crystalline $NbSb_2$ in a previous work.[20] For the polycrystalline $NbSb_2$, the angle between the magnetic field and the direction of the sintering pressure is noted as θ. When $\theta = 0°$, the position of the magnetic field is parallel to the direction of the sintering pressure. In the case that the carrier mobility is isotropic, the measured angle dependence of ρ should possess a circle shape.

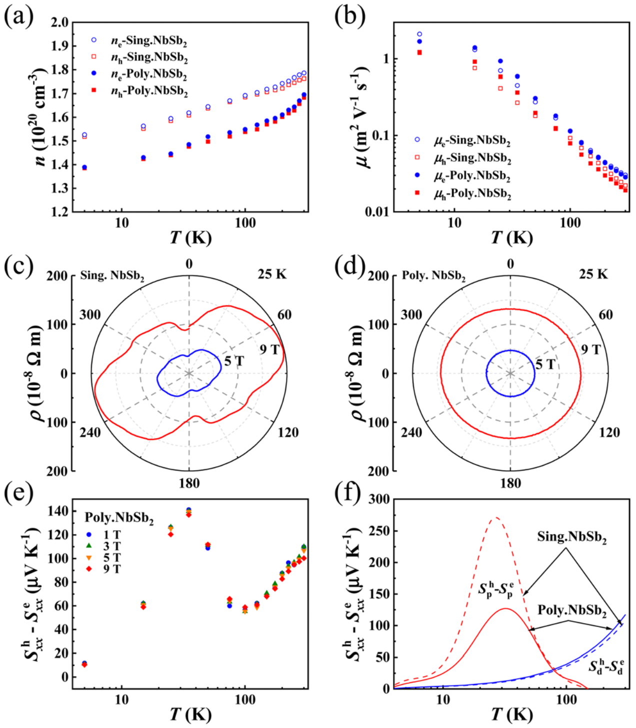

Fig. 4 (a) Carrier concentrations (n_{e} and n_{h}) and (b) carrier mobilities (μ_{e} and μ_{h}) of polycrystalline $NbSb_2$. Angular dependence of electrical resistivity ρ measured (c) along the *b*-axis of single-crystalline $NbSb_2$ and (d) the direction perpendicular the sintering pressure of polycrystalline $NbSb_2$ under 5 T and 9 T at 25 K. (e) Temperature dependence of the difference of Seebeck thermopower of electrons and holes ($S_{xx}^{\mathrm{h}} - S_{xx}^{\mathrm{e}}$) for polycrystalline $NbSb_2$ under different magnetic fields. (f) The difference of Seebeck thermopower of electrons and holes related to the charge carrier diffusion processes ($S_{\mathrm{d}}^{\mathrm{e}} - S_{\mathrm{d}}^{\mathrm{h}}$) and phonons ($S_{\mathrm{p}}^{\mathrm{e}} - S_{\mathrm{p}}^{\mathrm{h}}$) of polycrystalline and single-crystalline $NbSb_2$ at 5 T, respectively. The data of single-crystalline $NbSb_2$ are included in (a), (b), (e), and (f) for comparison.[20]

As shown in Fig. 4c, the measured angle dependence of ρ for single-crystalline $NbSb_2$ under 5 T or 9 T at 25 K has a typical two-fold rotational symmetry, which is similar to the crystal structure projection of $NbSb_2$ in the *ac*-plane (the inset in Fig. 2a). Under 9 T, the ρ at $\theta = 0°$ is just 94×10^{-8} Ω m, which is about 47% that at $\theta = 75°$ or 255° (198×10^{-8} Ω m). Since the carrier concentration is isotropic, the anisotropic ρ indicates that the carrier mobility of single-crystalline $NbSb_2$ varies considerably in the [010] crystal zone and that in the *bc*-plane is much lower than those in other planes. In contrast, the measured angle dependence of ρ in polycrystalline $NbSb_2$ at 25 K is nearly a circle (Fig. 4d). At 9 T, the maximum ρ (143×10^{-8} Ω m at around $\theta = 94°$ or 274°) is just about 1.09 times the minimum ρ (131×10^{-8} Ω m at around $\theta = 5°$ or 185°). This indicates the carrier mobility in the polycrystalline $NbSb_2$ has weak anisotropy, which is consistent with the randomly distributed grains shown in Fig. 2e. Thus, the measured carrier mobility of polycrystalline $NbSb_2$ should simultaneously include the contributions from all planes and grain boundaries. This can explain why the polycrystalline $NbSb_2$ has a high carrier mobility comparable with the single-crystalline $NbSb_2$ in the *bc*-plane.

Although the polycrystalline $NbSb_2$ has similar carrier mobilities to the single-crystalline $NbSb_2$, it has lower ($S^h_{xx} - S^e_{xx}$). As shown in Fig. 4e, under 9 T, the peak ($S^h_{xx} - S^e_{xx}$) of polycrystalline $NbSb_2$ is about 137 μV K^{-1}, which is about 57% that of single-crystalline $NbSb_2$.[20] The ($S^h_{xx} - S^e_{xx}$) includes two parts, termed as the ($S^h_d - S^e_d$) related to the diffusion process of charge carriers and the ($S^h_p - S^e_p$) related to the phonon-drag effect.[39] Fig. 4f shows the ($S^h_d - S^e_d$) and ($S^h_p - S^e_p$) of the polycrystalline $NbSb_2$, with the calculation details shown in the Supplementary Information. The former is comparable with that of single-crystalline $NbSb_2$, which is consistent with their similar carrier concentrations shown in Fig. 4a. However, the latter is much lower than that of single-crystalline $NbSb_2$, indicating the weaker phonon-drag effect in polycrystalline $NbSb_2$. The phonon-drag effect is caused by the interaction between the long-wavelength acoustic phonons and the carriers on the Fermi surface.[8] In polycrystals,[40,41] due to the grain boundary scattering, the relaxation time of the participating long-wavelength phonons is reduced, leading to the suppressed phonon-drag effect.

Fig. 5a and b show the temperature dependence and magnetic field dependence of thermal conductivity κ_{xx} for polycrystalline $NbSb_2$. As the temperature increases, the κ_{xx} first increases, reaching a peak around 35 K, and then decreases at higher temperature. Upon applying a magnetic field, κ_{xx} shows obvious reduction, especially below 30 K (Fig. 5a). This is caused by the suppressed carrier thermal conductivity κ_c under magnetic field. The κ_c and lattice thermal conductivity κ_l can be obtained by fitting the measured κ_{xx} according to an empirical formula[18,42,43]

$$\kappa_{xx}(B,T) = \kappa_l(T) + \frac{\kappa_c(0,T)}{1+\eta B^s} \tag{6}$$

where η and s are the two factors related to the thermal mobility and scattering mechanism, respectively. As shown in Fig. 5b, the fitting results agree well with the experimental data. The fitting parameters are shown in Table S1 (ESI†). The fitted κ_l values of polycrystalline $NbSb_2$ are plotted in the inset of Fig. 5a. The peak κ_l, appearing around 50 K, is 57.1 W m^{-1} K^{-1}, which is slightly lower than that of the single-crystalline $NbSb_2$ along the *b*-axis (64.3 W m^{-1} K^{-1} at 25 K).[20] At 300 K, the κ_{xx} is 23.5 W m^{-1} K^{-1}, which is still much higher than the state-of-the-art materials for Peltier refrigeration around room temperature, such as 0.7 W m^{-1} K^{-1} for Bi_2Te_3,[31] 0.7 W m^{-1} K^{-1} for Mg_3Bi_2,[5] and 0.34 W m^{-1} K^{-1} for Ag_2Se.[44] Under a high magnetic field, such as 9 T, κ_c is already very low (Fig. S8, ESI†), and κ_l dominates the measured κ_{xx}. Thus, reducing the overhigh κ_l is an important task for the investigation of $NbSb_2$ in the future.

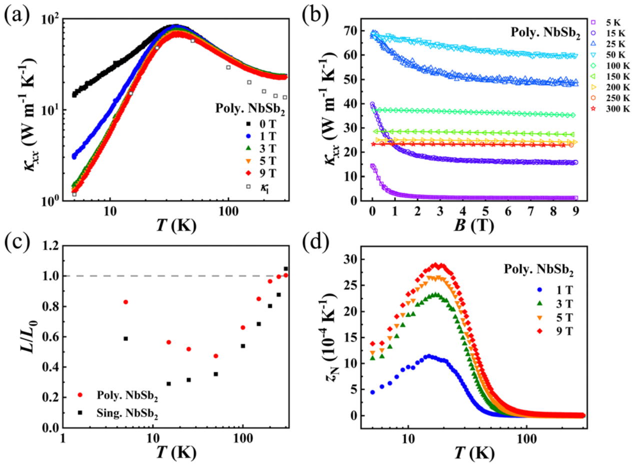

Fig. 5 (a) Temperature dependence of thermal conductivity κ_{xx} and lattice thermal conductivity κ_l under different magnetic fields for polycrystalline $NbSb_2$. (b) Magnetic field dependence of thermal conductivity κ_{xx} at different temperatures. The symbols are experimental data and the lines are the fitting curves. (c) The ratio of Lorentz number and the Sommerfeld value (L/L_0) for polycrystalline $NbSb_2$. (d) Temperature dependence of the Nernst figure-of-merit z_N for polycrystalline $NbSb_2$ under different magnetic fields. The data of single-crystalline $NbSb_2$ are included in (c) and (d) for comparison.[20]

Similar to most topological semimetal materials, the polycrystalline $NbSb_2$ also exhibits the abnormal Lorenz number L deviating off the classic Sommerfeld value L_0 below room temperature. Based on the fitted κ_c, the L can be calculated by using the Wiedemann–Franz law $L = \kappa_c/(\sigma_{xx}T)$. Fig. 5c plots the temperature dependence of L/L_0 for polycrystalline $NbSb_2$. With increasing temperature, the L/L_0 firstly decreases, reaching a minimum around 50 K, and then increases at higher temperature. The violation of the Wiedemann–Franz law at intermediate temperature range might be caused by the inelastic scattering,[45–47] while the upturn of L/L_0 below and above 50 K might be caused by the changed carrier scattering mechanism to the elastic scattering from the impurities and elastic electron–phonon scattering, respectively. Likewise, the L/L_0 of polycrystalline $NbSb_2$ is larger than that of single-crystalline $NbSb_2$, which might be caused by the dilution of inelastic scattering by grain boundary scattering.

Based on the S_{yx}, σ_{yy}, and κ_{xx}, the Nernst figure-of-merit z_N (= ${S_{yx}}^2\sigma_{yy}/\kappa_{xx}$) is calculated for polycrystalline $NbSb_2$. The detailed derivation process of z_N can be found in the Supplementary Information. Similar to the figure-of-merit z for thermoelectric materials, the z_N is also a parameter that is independent of the material's geometric factors. As shown in Fig. 5d, the z_N increases with increasing temperature, reaches a maximum around 18 K, and then decreases at higher temperature. Likewise, Fig. S9 (ESI†) shows that the z_N tends to saturate above 9 T, thus further increasing the magnetic field will not significantly increase z_N. The peak z_N of polycrystalline $NbSb_2$ is already much higher than all the polycrystalline thermomagnetic materials reported before (Fig. 1b and Fig. S10, ESI†), such as 0.93×10^{-4} K^{-1} for polycrystalline NbP under 9 T at 220 K[23] and 14.6×10^{-4} K^{-1} for polycrystalline Mn-doped Mg_3Bi_2 under 14 T at 14 K.[25] Actually, this value is also higher than those of many single-crystalline thermomagnetic materials reported before, such as 8×10^{-4} K^{-1} for $PtSn_4$ under 9 T at 10.3 K.[18] If the overhigh κ_l can be reduced without deteriorating the electrical transport properties, a higher z_N can be expected.

Based on the physical properties of polycrystalline $NbSb_2$, the maximum temperature difference (ΔT_{max}) and maximum specific heat pumping power (P_{max}) of a rectangular Ettingshausen refrigerator made of polycrystalline $NbSb_2$ can be estimated.[8,19] Under B = 9 T and T_c = 30 K, the ΔT_{max} of the $NbSb_2$-based Ettingshausen refrigerator with the thickness of 1 mm along the heat flow direction is about 0.9 K and the theoretical P_{max} is about 6.5 W g^{-1}. The latter value is much higher than the compression refrigerator with gas refrigerants (*e.g.* P_{max} = 0.05 W g^{-1} for He at 5 K, 0.12 W g^{-1} for H_2 at 26 K, and 1.01 W g^{-1} for N_2 at 93 K).[19] Thus, the polycrystalline $NbSb_2$ has a great potential to be used for Ettingshausen refrigeration.

Conclusions

In summary, we found that the polycrystalline $NbSb_2$ has an unsaturated Nernst thermopower S_{yx} of 396 μV K^{-1} under 9 T at 21 K and a giant Nernst power factor $(PF)_N$ of $\sim 1269 \times 10^{-4}$ W m^{-1} K^{-2} under 9 T at 28 K. The latter is almost an order of magnitude larger than the reported $(PF)_N$ of other polycrystalline thermomagnetic materials. The z_N of polycrystalline $NbSb_2$ is 28.5×10^{-4} K^{-1} under 9 T at 18 K, which is also a record-high value among the reported polycrystalline thermomagnetic materials. The superior $(PF)_N$ and z_N are attributed to the nearly identical electron and hole concentrations near the Fermi level, ultrahigh mobilities close to 1 m^2 V^{-1} s^{-1}, and the strong phonon-drag effect in low temperature ranges. Combining the low-cost and time-saving fabrication process, polycrystalline $NbSb_2$ is a very competitive candidate material for Ettingshausen refrigeration.

Experimental section

Sample synthesis

Polycrystalline $NbSb_2$ was synthesized *via* the solid-stated reaction and spark plasma sintering technique. The niobium powder (alfa, 99.99%) and antimony shot (alfa, 99.9999%) were encapsulated in a vacuum quartz tube and reacted at 1023 K for 48 h. The obtained product was ground into fine powders, loaded into a graphite mold and compacted by spark plasma sintering (SPS, SPS-725, Sojitz, Japan) in a vacuum. The sintering temperature was 1123 K and the sintering pressure was 65 MPa. The holding time at 1123 K is 10 min. The relative density of the sintered product was 98%.

Sample characterization

The phase composition was characterized by X-ray diffraction (XRD, D/max-2550 V, Rigaku, Japan). The elemental distribution was characterized by scanning electron microscopy (SEM, ZEISS supra-55, Germany) with energy dispersive X-ray spectroscopy (EDS, Oxford, UK). The bulk sample was cut into the strips of about $8 \times 2 \times 2$ mm^3 and $8 \times 2 \times 1$ mm^3 for electrical and thermal transport measurements under the magnetic field, respectively. All measurements were carried out on a physical property measurement system (PPMS, Quantum design, USA). The electrical resistivity and Hall resistivity were measured using a four-probe method and five-probe method, respectively. The Seebeck thermopower and Nernst thermopower were measured using the four-probe method on a standard thermal transport option (TTO) platform and a modified one, respectively. The details can be found in ref. 20. The S_{yx} data used to calculate Nernst power factor and Nernst figure-of-merit are obtained as $S_{yx} = [S_{yx}(+B) - S_{yx}(-B))]/2$ to eliminate the effects of contact misalignment.

Author contributions

P. L., P. Q., and X. S. designed the work. P. L. synthesized the samples and performed the transport property measurements with the help of J. X., and P. L. and T. D. analyzed the transport properties. L. C. provided helpful discussion. P. L., P. Q., and X. S. analyzed the data and wrote the manuscript.

Conflicts of interest

The authors declare no competing financial interests.

Acknowledgements

This work was supported by the National Natural Science Foundation of China (grants 52122213 and 91963208), the Shanghai Pilot Program for Basic Research-Chinese Academy of Science, Shanghai Branch (JCYJ-SHFY-2022-002), and the Shanghai Government (20JC1415100).

Notes and references

1 J. Chan, T. P. M. Alegre, A. H. Safavi-Naeini, J. T. Hill, A. Krause, S. Gröblacher, M. Aspelmeyer and O. Painter, *Nature*, 2011, **478**, 89–92.
2 C. Coats, J. S. Rogers and P. McIntyre, *IEEE Trans. Appl. Supercond.*, 2023, **33**, 1–5.
3 Y. Han and A. Zhang, *Sci. Rep.*, 2022, **12**, 2349.
4 J. Mao, G. Chen and Z. Ren, *Nat. Mater.*, 2021, **20**, 454–461.
5 J. Mao, H. Zhu, Z. Ding, Z. Liu, A. Gamage Geethal, G. Chen and Z. Ren, *Science*, 2019, **365**, 495–498.

6 Y. Qin, B. Qin, D. Wang, C. Chang and L. Zhao, *Energy Environ. Sci.*, 2022, **15**, 4527–4541.

7 Y. Zheng, X. Han, J. Yang, Y. Jing, X. Chen, Q. Li, T. Zhang, G. Li, H. Zhu, H. Zhao, G. J. Snyder and K. Zhang, *Energy Environ. Sci.*, 2022, **15**, 2374–2385.

8 H. J. Goldsmid, *Thermoelectric Refrigeration*, Plenum Press, Wembley, 1964.

9 H. J. Goldsmid, in *CRC Handbook of Thermoelectrics*, ed. D. M. Rowe, CRC Press LLC, Boca Raton, 1995, ch. 8, pp. 73–74.

10 K. F. Cuff, R. B. Horst, J. L. Weaver, S. R. Hawkins, C. F. Kooi and G. M. Enslow, *Appl. Phys. Lett.*, 1963, **2**, 145–146.

11 W. M. Yim and A. Amith, *Solid-State Electron.*, 1972, **15**, 1141–1165.

12 B. Madon, J. E. Wegrowe, H. J. Drouhin, X. Liu, J. Furdyna and G. A. Khodaparast, *J. Appl. Phys.*, 2016, **119**, 025701.

13 C. Fu, Y. Sun and C. Felser, *APL Mater.*, 2020, **8**, 040913.

14 X. Li, Z. Zhu and K. Behnia, *Adv. Mater.*, 2021, **33**, 2100751.

15 K. Behnia and H. Aubin, *Rep. Prog. Phys.*, 2016, **79**, 046502.

16 J. Xiang, S. Hu, M. Lyu, W. Zhu, C. Ma, Z. Chen, F. Steglich, G. Chen and P. Sun, *Sci. China: Phys., Mech. Astron.*, 2019, **63**, 237011.

17 P. Wang, C. Cho, F. Tang, P. Wang, W. Zhang, M. He, G. Gu, X. Wu, Y. Shao and L. Zhang, *Phys. Rev. B*, 2021, **103**, 045203.

18 C. Fu, S. N. Guin, T. Scaffidi, Y. Sun, R. Saha, S. J. Watzman, A. K. Srivastava, G. Li, W. Schnelle, S. S. P. Parkin, C. Felser and J. Gooth, *Research*, 2020, **2020**, 4643507.

19 Z. Chen, X. Zhang, J. Ren, Z. Zeng, Y. Chen, J. He, L. Chen and Y. Pei, *Nat. Commun.*, 2021, **12**, 3837.

20 P. Li, P. Qiu, Q. Xu, J. Luo, Y. Xiong, J. Xiao, N. Aryal, Q. Li, L. Chen and X. Shi, *Nat. Commun.*, 2022, **13**, 7612.

21 Y. Pan, B. He, T. Helm, D. Chen, W. Schnelle and C. Felser, *Nat. Commun.*, 2022, **13**, 3909.

22 C. Fu, S. N. Guin, S. J. Watzman, G. Li, E. Liu, N. Kumar, V. Süβ, W. Schnelle, G. Auffermann, C. Shekhar, Y. Sun, J. Gooth and C. Felser, *Energy Environ. Sci.*, 2018, **11**, 2813–2820.

23 W. Liu, Z. Wang, J. Wang, H. Bai, Z. Li, J. Sun, X. Zhou, J. Luo, W. Wang, C. Zhang, J. Wu, Y. Sun, Z. Zhu, Q. Zhang and X. Tang, *Adv. Funct. Mater.*, 2022, **32**, 2202143.

24 T. Feng, P. Wang, Z. Han, L. Zhou, W. Zhang, Q. Liu and W. Liu, *Adv. Mater.*, 2022, **34**, 2200931.

25 T. Feng, P. Wang, Z. Han, L. Zhou, Z. Wang, W. Zhang, Q. Liu and W. Liu, *Energy Environ. Sci.*, 2023, **16**, 1560–1568.

26 S. J. Watzman, T. M. McCormick, C. Shekhar, S.-C. Wu, Y. Sun, A. Prakash, C. Felser, N. Trivedi and J. P. Heremans, *Phys. Rev. B*, 2018, **97**, 161404(R).

27 C. Shekhar, A. K. Nayak, Y. Sun, M. Schmidt, M. Nicklas, I. Leermakers, U. Zeitler, Y. Skourski, J. Wosnitza, Z. Liu, Y. Chen, W. Schnelle, H. Borrmann, Y. Grin, C. Felser and B. Yan, *Nat. Phys.*, 2015, **11**, 645–649.

28 H. Wang, Z. Zhou, J. Ying, Z. Xiang, R. Wang, A. Wang, Y. Chai, M. He, X. Lu, G. Han, Y. Pan, G. Wang, X. Zhou and X. Chen, *Adv. Mater.*, 2023, **35**, 2206941.

29 R. T. Delves, *Rep. Prog. Phys.*, 1965, **28**, 249–289.

30 X. Liu, T. Xing, P. Qiu, T. Deng, P. Li, X. Li, X. Li and X. Shi, *J. Materiomics*, 2023, **9**, 345–352.

31 R. Deng, X. Su, Z. Zheng, W. Liu, Y. Yan, Q. Zhang, V. P. Dravid, C. Uher, M. G. Kanatzidis and X. Tang, *Sci. Adv.*, 2018, **4**, eaar5606.

32 Y. Wu, P. Qiu, Y. Yu, Y. Xiong, T. Deng, O. Cojocaru-Mirédin, M. Wuttig, X. Shi and L. Chen, *J. Materiomics*, 2022, **8**, 1095–1103.

33 Q. Xu, C. Ming, T. Xing, P. Qiu, J. Xiao, X. Shi and L. Chen, *Mater. Today Phys.*, 2021, **19**, 100417.

34 Z. Gao, Q. Yang, P. Qiu, T.-R. Wei, S. Yang, J. Xiao, L. Chen and X. Shi, *Adv. Energy Mater.*, 2021, **11**, 2100883.

35 Q. Yang, S. Yang, P. Qiu, L. Peng, T.-R. Wei, Z. Zhang, X. Shi and L. Chen, *Science*, 2022, **377**, 854–858.

36 M. Jin, X. Bai, R. Zhang, L. Zhou and R. Li, *J. Inorg. Mater.*, 2021, **37**, 101–106.

37 R. T. Delves, *Br. J. Appl. Phys.*, 1964, **15**, 105–106.

38 L. Guo, Y. K. Liu, G. Y. Gao, Y. Y. Huang, H. Gao, L. Chen, W. Zhao, W. Ren, S. Y. Li, X. G. Li, S. Dong and R. K. Zheng, *J. Appl. Phys.*, 2018, **123**, 155103.

39 F. J. Blatt, P. A. Schroeder, C. L. Foiles and D. Greig, *Thermoelectric power of metals*, Plenum Press, New York and London, 1976.

40 J. Zhou, B. Liao, B. Qiu, S. Huberman, K. Esfarjani, M. S. Dresselhaus and G. Chen, *Proc. Natl. Acad. Sci. U. S. A.*, 2015, **112**, 14777–14782.

41 M. Pokharel, H. Zhao, K. Lukas, Z. Ren, C. Opeil and B. Mihaila, *MRS Commun.*, 2013, **3**, 31–36.

42 R. Ocaña and P. Esquinazi, *Phys. Rev. B*, 2002, **66**, 064525.

43 F. Han, N. Andrejevic, T. Nguyen, V. Kozii, Q. T. Nguyen, T. Hogan, Z. Ding, R. Pablo-Pedro, S. Parjan, B. Skinner, A. Alatas, E. Alp, S. Chi, J. Fernandez-Baca, S. Huang, L. Fu and M. Li, *Nat. Commun.*, 2020, **11**, 6167.

44 J. Liang, P. Qiu, Y. Zhu, H. Huang, Z. Gao, Z. Zhang, X. Shi and L. Chen, *Research*, 2020, **2020**, 6591981.

45 J. Gooth, F. Menges, N. Kumar, V. Subeta, C. Shekhar, Y. Sun, U. Drechsler, R. Zierold, C. Felser and B. Gotsmann, *Nat. Commun.*, 2018, **9**, 4093.

46 A. Jaoui, B. Fauqué, C. W. Rischau, A. Subedi, C. Fu, J. Gooth, N. Kumar, V. Süß, D. L. Maslov, C. Felser and K. Behnia, *npj Quantum Mater.*, 2018, **3**, 64.

47 N. Kumar, Y. Sun, M. Nicklas, S. J. Watzman, O. Young, I. Leermakers, J. Hornung, J. Klotz, J. Gooth, K. Manna, V. Süß, S. N. Guin, T. Förster, M. Schmidt, L. Muechler, B. Yan, P. Werner, W. Schnelle, U. Zeitler, J. Wosnitza, S. S. P. Parkin, C. Felser and C. Shekhar, *Nat. Commun.*, 2019, **10**, 2475.